Robust Perspective-n-Crater for Crater-based Camera Pose Estimation

Sofia McLeod[1] Chee Kheng Chng[1] Tatsuharu Ono[2] Yuta Shimizu[3]
Ryodo Hemmi[3], Lachlan Holden[1] Matthew Rodda[1]
Feras Dayoub[1] Hirdy Miyamoto[3] Yukihiro Takahashi[2] Yasuko Kasai[4] Tat-Jun Chin[1]*
[1]The University of Adelaide, [2]Hokkaido University
[3]University of Tokyo, [4]Tokyo Institute of Technology

Abstract

Lunar survey missions require accurate estimation of satellite and/or sensor pose (position and attitude) to achieve precise surface measurement. Crater-based pose estimation (CBPE) holds promise to achieve the desired accuracy. However, current pose estimation methods suffer from one or more weaknesses, such as loose coupling of position and attitude optimisation, not accounting for wrong crater matches, and using geometrically invalid objective functions for estimation. To conclusively address these drawbacks, we develop a robust perspective-n-crater pose estimation method that employs geometrically meaningful and information-rich elliptical representation of craters, in combination with M-estimators to account for incorrect crater identifications. To enable evaluation, we construct an extensive labelled dataset of synthetic lunar images taken under diverse conditions over the Moon's surface. Results on the dataset demonstrate that our work addresses the drawbacks of previous methods and raises the achievable accuracy of CBPE. As another contribution, we will also release our dataset to stimulate further research.

1. Introduction

In recent years, the surge in human activity in cislunar space has led to over 30 planned missions to the Moon by 2030, encompassing flybys, orbiting, and landings. A critical aspect of these ventures is spacecraft navigation, which has seen significant advancements [4, 10, 14, 21, 33].

Increasingly, vision-based navigation systems are being adopted for these missions [4, 21]. The preference for these systems is due in part to the availability of mature camera payloads for space exploration missions. In particular, terrain relative navigation (TRN) [14], where the natural landmarks observed on a planetary body (*e.g.*, Moon, Mars, asteroids) are used to localise and orient a spacecraft relative to a reference frame on the body, has met success in recent years, *e.g.*, in the OSIRIS-REx sample return mission [19] and the landing of the Perseverance rover on Mars [24].

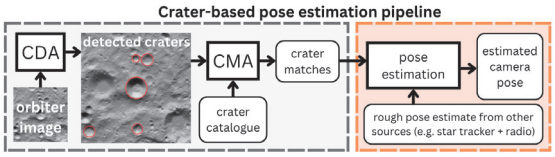

Figure 1. A representative CBPE pipeline.

Absolute camera pose for cislunar-located spacecraft can be determined from a single image provided there is a known association between the 2D image observation and the corresponding 3D landmark in the lunar reference frame. Prior lunar missions have captured highly detailed data on the Moon's topographical composition [26, 30] which in turn has allowed for the creation of high-resolution digital elevation maps (DEM) [25] and crater catalogues [29]. Given that craters are detectable 2D features in the image plane with known 3D locations in the lunar reference frame, this has motivated the development of crater-based pose estimation (CBPE) for cislunar localisation.

As depicted in Figure 1, existing CBPE algorithmic pipelines broadly consist of a crater detection algorithm (CDA), a crater matching algorithm (CMA) and a final pose estimation step. Crater detection and crater matching represent considerable challenges as they are prone to producing noisy crater detections and false crater matches (outliers) which can result in inaccurate or outright wrong pose estimates. For this reason, CDA and CMA have been the primary focus of CBPE research. Comparatively, the pose estimation step of the pipeline has received less attention.

The pose estimation step in recently proposed CBPE pipelines suffers from one or more weaknesses, *e.g.*, decoupled estimation of position and orientation thereby leading to suboptimal 6 degree-of-freedom (DoF) pose estimate [4, 6, 15], not accounting for outliers from CMA [4, 6, 36],

*SmartSat CRC Professorial Chair of Sentient Satellites.

and using geometrically invalid cost functions for estimation [2, 21, 37, 38]. A notable example of the latter case is solving the perspective-n-point (PnP) problem to estimate pose from 2D-3D crater matches [2, 21, 37, 38], which essentially assumes that a 2D imaged ellipse produces a line-of-sight vector to the centre of the corresponding 3D crater rim, which is generally not true [4] (see Figure 2a). As we will show in Section 5, this could limit the CBPE accuracy.

Additionally, there have been few studies that comprehensively evaluated different CBPE pipelines. A major factor is the lack of publicly available data (*e.g.*, lunar surface images) that is labelled (*e.g.*, with ground truth CDA/CMA results or camera poses). This has made it difficult to compare and benchmark different CBPE solutions.

1.1. Contributions

To address the weaknesses of pose estimation methods in existing CBPE pipelines, we propose a robust *perspective-n-crater (PnC)* approach that estimates 6DoF camera pose from crater correspondences. Our method minimises the reprojection error of craters represented in a geometrically meaningful and information-rich elliptical format, with the use of M-estimators to account for outlier crater matches. We conclusively demonstrate that our work addresses the drawbacks of previous methods and makes significant improvements to the overall CBPE accuracy.

To comprehensively evaluate the performance of pose estimators in the context of CBPE, we produced CRESENT: a CRatEr-baSed pose estimation datasEt for cisluNar-located spacecrafT[1]. CRESENT is an extensive dataset consisting of synthetically generated images with corresponding ground truth camera poses taken above lunar regions of scientific interest at varying angles off nadir. Given a crater catalogue, ground truth crater locations can be obtained and used to provide CDA/CMA results.

2. Related work

Here, we further survey existing methods that contribute to CBPE and motivate our work.

2.1. CDA

The input to a CBPE pipeline is an image taken of the lunar surface which is then passed to a CDA to return the location and elliptical rim shape of the detected craters on the image plane. There are more than 100 CDAs listed in survey papers [7, 31, 35], and recent developments in CDAs which used machine learning [9, 16, 32, 34]. CDAs need to be able to detect as many craters as possible with high ellipse fitting precision to yield accurate pose estimates, hence, this is an active research topic in CBPE research [2, 6, 12, 42].

[1]CRESENT will be released publicly.

2.2. CMA

After craters have been detected by the CDA, the imaged craters are passed to a CMA and matched to known craters in a crater catalogue. The crater catalogue used by recent crater-based pose estimation algorithms [2, 4, 6, 8] is Robbins' crater catalogue [29], consisting of 1.3 million manually identified craters describing the location and shape of each crater. CMA approaches have varied from context matching to cross-correlation matching to state-of-the-art descriptor matching [3, 4, 12, 13, 21, 27, 39]. While there has been significant progress made in CMA development, CMAs are still prone to producing outlier crater matches which if not dealt with, can result in bad pose estimates.

2.3. Pose estimation from crater matches

While there has been extensive research into CDA and CMA development, there have been fewer studies on pose estimation algorithms for CBPE. Often, pose estimation methods are integrated into CBPE pipelines without strong conceptual or empirical justifications (more details below), which raises questions on the achievable accuracy.

Rather than estimating the 6DoF pose, many CBPE pipelines restrict the estimated DoF by assuming known attitude [4, 6], known altitude and attitude [15, 36] or restrict the application to a landing scenario which assumes coplanar craters [20]. Christian *et al*. have produced a state-of-the-art CBPE pipeline [4] with a position estimation step solved in a least squares (LS) sense using verified crater matches and known attitude from a star tracker. While star trackers can be accurate in the range of arcseconds [18], without the ability to refine the attitude, any error introduced by the star tracker will directly affect the position and observed surface accuracy. Another drawback of this method is that the LS solver does not account for outlier crater matches. While Doppenberg [8] built on this method by implementing random sample consensus (RANSAC) [11] to account for outliers, the base metric still directly solves the position without the option to refine for attitude.

As far as we are aware, there have been four recent CBPE pipelines that have applied the PnP algorithm to solve for 6DoF pose [2, 21, 37, 38]. While these methods allow for the estimation of both position and attitude estimates, the point representation used by PnP assumes the 3D ellipse centre of the catalogued crater projects to the centre of the corresponding 2D imaged ellipse, which is generally not true (see Figure 2a). Zhu *et al*. indirectly accounts for this in their weighted POSIT algorithm by acknowledging the anisotropic, correlated and non-identical characteristics of the craters' localisation errors [42]. However, in scenarios where few craters are detected or the majority of craters are given low weightings, the pose accuracy will suffer. A further drawback of these methods is the substantial amount of valuable navigation information lost from reducing the

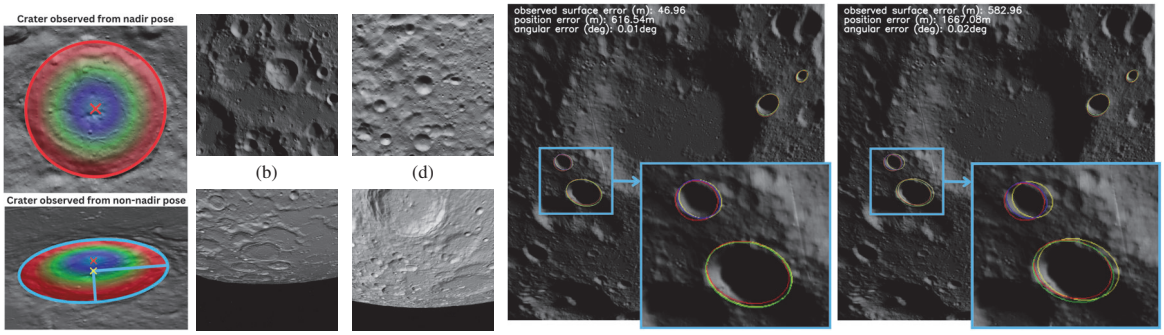

(a) (b) (c) (d) (e) (f) EP (g) PnP

Figure 2. (a) The centre of a crater ellipse (red cross) does not necessarily project to the centre of the ellipse (yellow cross) that corresponds to the crater rim when viewed from a non-nadir pose. (b) - (e) Lunar dataset regions produced using PANGU Planet Surface Simulation Software developed by the Space Technology Centre at the University of Dundee, Scotland. (b) North Pole (c) South Pole (d) region of highest crater density (e) region of lowest crater density. (f)(g) Problem instances with ground truth crater locations (green), noisy crater locations (red) and incorrectly matched craters (blue), reprojected with optimised pose (yellow) from the EP (Sec. 4.1) (f) and PnP (Sec. 3.3) (g) metrics, yielding observed surface errors of 46.96 m and 582.96 m respectively.

elliptical representation of a crater to a single point.

3. Preliminaries

In this section, we provide important background information before describing the proposed method in Sec. 4.

3.1. Crater imaging

The rim of a real-world crater can be approximated as a 2D ellipse (1) on a local plane on the Moon's surface. The 2D ellipse can be represented as a conic

$$\mathbf{D} = \begin{bmatrix} J & I/2 & Q/2 \\ I/2 & O & S/2 \\ Q/2 & S/2 & U \end{bmatrix} \tag{1}$$

where the values in $\mathbf{D}$ are extracted from the structure of the crater as compiled in a crater catalogue, *e.g.*, [29]. The normal of the local plane and selenographic coordinates of the crater centre $\mathbf{p}_M$ can also be derived from the data in the crater catalogue. This allows to set up a local east-north-up (ENU) frame $\mathbf{T} = \begin{bmatrix} \mathbf{e} & \mathbf{n} & \mathbf{u} \end{bmatrix}$ centred at $\mathbf{p}_M$ [4].

It follows that the transformation relating a homogeneous 2D point $\bar{\mathbf{q}}_E$ on the crater ellipse to the corresponding homogeneous 3D point $\bar{\mathbf{q}}_M$ in the selenographic frame is

$$\bar{\mathbf{q}}_M = \begin{bmatrix} \mathbf{L} \\ \mathbf{k}^T \end{bmatrix} \bar{\mathbf{q}}_E, \tag{2}$$

where

$$\mathbf{k} = \begin{bmatrix} 0 \\ 0 \\ 1 \end{bmatrix} \quad \mathbf{L} = \begin{bmatrix} \mathbf{TS} \\ \mathbf{p}_M \end{bmatrix} \quad \mathbf{S} = \begin{bmatrix} \mathbf{I}_{2\times 2} \\ \mathbf{0}_{1\times 2} \end{bmatrix}. \tag{3}$$

Let the pose of a camera observing the lunar surface be

$$(\mathbf{R}, \mathbf{r}_M), \tag{4}$$

where $\mathbf{R} \in SO(3)$ is the rotation from the selenographic frame to the camera frame and $\mathbf{r}_M$ is the camera's position in the selenographic frame. The camera projection matrix

$$\mathbf{P} = \mathbf{K}[\mathbf{R}|\mathbf{r}_C] \tag{5}$$

allows to perspectively project a 3D point expressed in the selenographic frame to the image frame, where $\mathbf{K} \in \mathbb{R}^{3\times 3}$ is the calibrated camera intrinsic matrix, and

$$\mathbf{r}_C = -\mathbf{R} \cdot \mathbf{r}_M. \tag{6}$$

We can thus determine the homography $\mathbf{H}$ between the camera's image plane and the crater's local plane as

$$\mathbf{H} = \mathbf{P} \begin{bmatrix} \mathbf{L} \\ \mathbf{k^T} \end{bmatrix}. \tag{7}$$

The 2D conic $\mathbf{D}$ of the crater defined in the local crater plane, and the 2D conic $\mathbf{A}$ which defines an ellipse that outlines the crater's rim observed in the image taken under camera pose $(\mathbf{R}, \mathbf{r}_M)$, can be related by

$$\mathbf{A}^{-1} \propto \mathbf{H} \cdot \mathbf{D}^{-1} \cdot \mathbf{H}^T. \tag{8}$$

To simplify subsequent notations, we summarise (8) as

$$\mathbf{A} := g(\mathbf{R}, \mathbf{r}_M, \mathbf{D}). \tag{9}$$

3.2. Position estimation in the known attitude case

Let $\mathbb{A} = \{\mathbf{A}_i\}_{i=1}^N$ be detected 2D ellipses resulting from applying a CDA on an input image. Let $\mathbb{D} = \{\mathbf{D}_i\}_{i=1}^N$ be

the local plane conics of catalogue craters determined by a CMA to correspond to the observed craters $\mathbb{A}$. Our aim is to estimate the camera pose $(\mathbf{R}, \mathbf{r}_M)$ of the input image based on the crater correspondences $\mathcal{C} = (\mathbb{A}, \mathbb{D})$, which is noisy and contaminated with false correspondences (outliers).

Assuming known camera attitude $\mathbf{R}$, Christian *et al*. [4] construct the system of linear equations

$$\begin{bmatrix} \mathbf{S}^T{\mathbf{T}_1}^T\mathbf{B}_1 \\ \vdots \\ \mathbf{S}^T{\mathbf{T}_N}^T\mathbf{B}_N \end{bmatrix} \mathbf{r}_M = \begin{bmatrix} \mathbf{S}^T{\mathbf{T}_1}^T\mathbf{B}_1\mathbf{p}_{M_1} - \hat{\mathbf{s}_1}\mathbf{S}^T\mathbf{D}_1\mathbf{k} \\ \vdots \\ \mathbf{S}^T{\mathbf{T}_N}^T\mathbf{B}_N\mathbf{p}_{M_N} - \hat{\mathbf{s}_N}\mathbf{S}^T\mathbf{D}_N\mathbf{k} \end{bmatrix} \tag{10}$$

and solve for $\mathbf{r}_M$ using linear LS, where

$$\hat{\mathbf{s}_i} = \frac{\text{vec}(\mathbf{S}^T\mathbf{D}_i\mathbf{S})^T\text{vec}(\mathbf{S}^T{\mathbf{T}_i}^T\mathbf{B}_i\mathbf{T}_i^T\mathbf{S})}{\text{vec}(\mathbf{S}^T\mathbf{D}_i\mathbf{S})^T\text{vec}(\mathbf{S}^T\mathbf{D}_i\mathbf{S})} \tag{11}$$

$$\mathbf{B}_i = \mathbf{R}^T\mathbf{K}^T\mathbf{A}_i\mathbf{K}\mathbf{R}. \tag{12}$$

However, solving for position without jointly estimating the attitude can be problematic, since errors in the attitude will cause errors in the estimated position, leading to overall suboptimal 6DoF pose estimates, as we will show in Sec. 5.

Moreover, the LS method does not account for outliers, though the method can be extended with RANSAC [8].

3.3. Estimating pose through PnP

CPBE pipelines that invoke PnP minimise the reprojection error of the crater centres from the crater catalogue to the ellipse centres of the detected crater ellipses [2, 21, 37, 38].

The crater centre is projected onto the image plane as

$$\bar{\mathbf{p}}_c = \mathbf{P}\bar{\mathbf{p}}_M, \tag{13}$$

where $\mathbf{P}$ is the camera projection matrix (5), $\bar{\mathbf{p}}_M = [\mathbf{p}_M^T\ 1]^T$ is the homogeneous version of the selenographic crater centre coordinates $\mathbf{p}_M$, and $\bar{\mathbf{p}}_c = [\mathbf{p}_c^T\ 1]^T$ is the homogeneous version of the projected crater centre on the image plane $\mathbf{p}_c = [p_x, p_y]$. For brevity let h be the function

$$\mathbf{p}_c = h(\mathbf{R}, \mathbf{r}_M, \mathbf{p}_M), \tag{14}$$

that obtains the projected image coordinates of a crater centre under camera pose $(\mathbf{R}, \mathbf{r}_M)$.

Let $\mathbb{J} = \{\mathbf{p}_{c,i}\}_{i=1}^N$ be a set of crater centres observed in the input image, and $\mathbb{K} = \{\mathbf{p}_{M,i}\}_{i=1}^N$ be the centres of corresponding craters in selenographic frame. To estimate the camera pose underlying the image, PnP solves

$$\min_{(\mathbf{R},\mathbf{r}_M)\in SE(3)} \sum_{i=1}^{N} \left\| h(\mathbf{R}, \mathbf{r}_M, \mathbf{p}_{M,i}) - \mathbf{p}_{c,i} \right\|_2, \tag{15}$$

which can be achieved using a PnP solver, *e.g*., [17].

While $\mathbb{K}$ are the centres of $\mathbb{D}$, the centres of $\mathbb{A}$ do not necessarily equate to $\mathbb{J}$, as illustrated in Fig. 2a. PnP-based methods [2, 21, 37, 38] that take the centres of $\mathbb{A}$ as the observed centres of $\mathbb{D}$ run the risk of significant errors in the estimated pose, as we will show in Sec. 5.

4. Perspective-n-Crater

To address the shortcomings of the methods in Sections 3.2 and 3.3, we propose a robust PnC approach that can estimate 6DoF camera poses. As mentioned in Section 2.3, previous CBPE methods that took ellipse shape into account have considered more restricted cases (*e.g*., position estimation only [4], assumes all craters are coplanar [20]).

As before, the input to our method is a set of noisy and outlier prone crater correspondences $\mathcal{C} = (\mathbb{A}, \mathbb{D})$, where $\mathbb{A} = \{\mathbf{A}_i\}_{i=1}^N$ are 2D ellipses in the input image detected by a CDA, and $\mathbb{D} = \{\mathbf{D}_i\}_{i=1}^N$ are the local plane conics of catalogue craters determined to be corresponding to $\mathbb{A}$ by a CMA. In its general form, the proposed PnC solves

$$\begin{aligned} \min_{(\mathbf{R},\mathbf{r}_M)\in SE(3)} \quad & \sum_{i=1}^{N} d\left[g(\mathbf{R}, \mathbf{r}_M, \mathbf{D}_i), \mathbf{A}_i\right] \\ \text{subject to} \quad & \angle(\mathbf{R}, \mathbf{R}^\dagger) \leq \delta, \\ & \|\mathbf{r}_M - \mathbf{r}_M^\dagger\|_2 \leq \gamma, \end{aligned} \tag{16}$$

where d is an ellipse error function that measures the discrepancy between the (perspective) image projection of $\mathbf{D}_i$ and the observed ellipse $\mathbf{A}_i$, while $\angle(\cdot,\cdot)$ is a suitable metric (*e.g*., chordal distance) between two rotation matrices.

Another departure from previous methods is the inclusion of constraints in (16) that allows to leverage *a priori* known attitude $\mathbf{R}^\dagger$ and position $\mathbf{r}_M^\dagger$, respectively with uncertainty δ and γ. Such prior information can be obtained from other positioning capabilities such as onboard star trackers [18] and radio ranging [21, 22].

PnC is related to the perspective-n-ellipsoid (PnE) problem in robotic vision [43], which aims to estimate camera pose from observations of objects that can be bounded within ellipsoids. Since ellipsoids are imaged as ellipses, ellipse error functions used in PnE are also applicable to PnC. Nonetheless the different types of reference 3D objects demand a careful selection of ellipse errors for PnC.

4.1. Ellipse error functions for PnC

The conic parameters of a 2D ellipse, *i.e*., $\mathbf{A}_i$ or the result of the projection $g(\mathbf{R}, \mathbf{r}_M, \mathbf{D}_i)$, can be distilled into five geometrically meaningful parameters (x, y, a, b, θ), where $\mathbf{x} = [x, y]$ is the ellipse centre, $\mathbf{r} = [a, b]$ are the lengths of the semi-major and semi-minor axes of the ellipse, and θ is the angle of orientation on the plane; see Sec. 8 of the supplementary material for the distillation process.

Given two sets of ellipse parameters $\mathbf{e} = (x, y, a, b, \theta)$ and $\mathbf{e}' = (x', y', a', b', \theta)$, the following ellipse error functions are applicable to PnC:

- **Ellipse centre distance (ED):** We compare the centre of the projected crater ellipse, with the centre of the detected

crater ellipse, as follows:

$$d = \left\| \begin{bmatrix} x \\ y \end{bmatrix} - \begin{bmatrix} x' \\ y' \end{bmatrix} \right\|_2 . \tag{17}$$

- **Ellipse parameter distance (EP):** The EP takes the difference between the ellipse parameters directly

$$d = \|\mathbf{e} - \mathbf{e}'\|_2 \tag{18}$$

- **Ellipse characteristic point distance (ECP):** The five characteristic points (CPs) of an ellipse $\mathbf{e}$ are

$$p_0 = \begin{bmatrix} x & y \end{bmatrix}^T , \tag{19}$$

$$p_1 = \begin{bmatrix} x + a\cos(\theta) & y + a\sin(\theta) \end{bmatrix}^T , \tag{20}$$

$$p_2 = \begin{bmatrix} x - b\sin(\theta) & y + b\cos(\theta) \end{bmatrix}^T , \tag{21}$$

$$p_3 = \begin{bmatrix} x - a\cos(\theta) & y - a\sin(\theta) \end{bmatrix}^T , \tag{22}$$

$$p_4 = \begin{bmatrix} x + b\sin(\theta) & y - b\cos(\theta) \end{bmatrix}^T . \tag{23}$$

Given the CPs from two ellipses, the ECP [40] is

$$d = \left(\sum_{\ell=0}^{4} (p_\ell - p'_\ell)^2 \right)^{1/2} . \tag{24}$$

- **Level set distance (L_Set):** The level set distance is a cost function based on level set sampling [43]. The general quadric equation of an ellipse is

$$\Upsilon(\mathbf{x_s}) = (\mathbf{x_s} - \mathbf{x})^T \mathbf{V} \begin{bmatrix} \frac{1}{a^2} & 0 \\ 0 & \frac{1}{b^2} \end{bmatrix} \mathbf{V}^T (\mathbf{x_s} - \mathbf{x}) \tag{25}$$

where $\mathbf{V}$ is the rotation matrix for the ellipse's angle of orientation θ. The distance is calculated as a summation of the distances from regularly sampling a finite set of n points along the level curves of the first ellipse

$$d = \sum_{j=1}^{n} (\Upsilon(\mathbf{x_j}) - \Upsilon'(\mathbf{x_j}))^2 . \tag{26}$$

- **Wasserstein distance (Wass):** The Wasserstein distance proposed by Zins *et al.* [43], is used to compare two 2D Gaussian distributions. An ellipse is represented as a Gaussian distribution $\mathcal{N}(\mathbf{x}, \mathbf{\Sigma})$ where

$$\mathbf{\Sigma}^{-1} = \mathbf{V} \begin{bmatrix} \frac{1}{a^2} & 0 \\ 0 & \frac{1}{b^2} \end{bmatrix} \mathbf{V}^T \tag{27}$$

with the Wasserstein distance calculated as follows

$$d = \|\mathbf{x} - \mathbf{x}'\|_2^2 + Tr(\mathbf{\Sigma} + \mathbf{\Sigma}' - 2(\mathbf{\Sigma}^{\frac{1}{2}} \mathbf{\Sigma}' \mathbf{\Sigma}^{\frac{1}{2}})^{\frac{1}{2}}) \tag{28}$$

- **Gaussian angle distance (Gauss_Ang):** The Gaussian angle is the distance between two bivariate Gaussian distributions [4] and is defined as follows

$$d = \cos^{-1}(G), \tag{29}$$

where $G = \frac{4\sqrt{|\mathbf{\Sigma}^{-1}||\mathbf{\Sigma}'^{-1}|}}{|\mathbf{\Sigma}^{-1} + \mathbf{\Sigma}'^{-1}|} \exp\Big[- \frac{1}{2}(\mathbf{x} - \mathbf{x}')^T \mathbf{\Sigma}^{-1} (\mathbf{\Sigma}^{-1} + \mathbf{\Sigma}'^{-1})^{-1} \mathbf{\Sigma}'^{-1} (\mathbf{x} - \mathbf{x}') \Big]$

Section 5 will comprehensively evaluate the different ellipse distances for PnC-based camera pose estimation.

4.2. Optimisation algorithm

PnC is a non-linear least squares (NLLS) problem that can be solved using existing NLLS solvers. In this work, we used SciPy's Optimize with L-BFGS-B method, which is a second-order Quasi-Newton method used to solve large nonlinear optimisation problems [5]. The package supports numerical differentiation and nonlinear constraints, which allow convenient implementation of (16).

4.3. M-estimators for robust PnC

To account for outliers in $\mathcal{C}$, we employed M-estimators for PnC. Problem (16) is modified to become

$$\min_{(\mathbf{R}, \mathbf{r}_M) \in SE(3)} \sum_{i=1}^{N} \rho \left\{ d \left[g(\mathbf{R}, \mathbf{r}_M, \mathbf{D}_i), \mathbf{A}_i \right] \right\} , \tag{30}$$

where ρ is a robust loss function called an M-estimator[2]. We adopted Tukey's biweight [41] in our work,

$$\rho(d) = \begin{cases} (\epsilon^2/6)(1 - \left[1 - (d/\epsilon)^2\right]^3) & \text{if } |d| \leq \epsilon \\ (\epsilon^2/6) & \text{otherwise,} \end{cases} \tag{31}$$

where ϵ is a positive, user defined inlier threshold. Intuitively, ρ ignores the contribution of crater matches whose ellipse distances are greater than ϵ.

To solve (30), we applied the iteratively reweighted least squares (IRLS) algorithm [41]. Starting from an initial $(\mathbf{R}^{(0)}, \mathbf{r}_M^{(0)})$, at each iteration t, IRLS obtains the error

$$d_i^{(t)} = d \left[g(\mathbf{R}^{(t)}, \mathbf{r}_M^{(t)}, \mathbf{D}_i), \mathbf{A}_i \right] \tag{32}$$

of each datum based on the current estimate $(\mathbf{R}^{(t)}, \mathbf{r}_M^{(t)})$, and computes the weight of each datum using the function

$$w_i^{(t)} = w(d_i^{(t)}) = \rho'(d_i^{(t)}) / d_i^{(t)} , \tag{33}$$

where ρ' is the derivative of ρ. IRLS then updates the parameters to $(\mathbf{R}^{(t+1)}, \mathbf{r}_M^{(t+1)})$ by solving the weighted LS

$$\min_{(\mathbf{R}, \mathbf{r}_M) \in SE(3)} \sum_{i=1}^{N} w_i^{(t)} d \left[g(\mathbf{R}, \mathbf{r}_M, \mathbf{D}_i), \mathbf{A}_i \right]^2 , \tag{34}$$

which we achieved using the NLLS solver (Sec. 4.2). The alternation is conducted until convergence. Algorithm 1 describes the proposed robust PnC based on M-estimation.

[2]For brevity we did not show constraints in (30), but readers should be reminded that that the constraints in (16) apply to all problems in Sec. 4.3.

Algorithm 1 Robust PnC based on M-estimation.

Require: $\mathbb{D} = \{\mathbf{D}_i\}_{i=0}^{N}$, $\mathbb{A} = \{\mathbf{A}_i\}_{i=0}^{N}$, initial attitude estimate $\mathbf{R}^{(0)}$, initial position estimate $\mathbf{r}_M^{(0)}$, convergence threshold λ, maximum number of iterations T,

$w_i^{(0)} = 1$ for all i
$o^{(0)} \leftarrow$ minimised value of (34) at $t = 0$
for t in range $1...T$ **do**
  $\mathbf{R}^{(t)}, \mathbf{r}_M^{(t)} \leftarrow$ minimiser from (34)
  $o^{(t)} \leftarrow$ minimised value from (34)
  if $|o^{(t)} - o^{(t-1)}| \leq \lambda$ **then**
    return $\mathbf{R}^{(t)}, \mathbf{r}_M^{(t)}$
  end if
end for

5. Results

This section will outline the proposed CRESENT dataset and results of benchmarking different CBPE methods on the dataset. Methods that were compared consist of the 3DoF LS solver (3DoF_LS) (Section 3.2), PnP (Section 3.3), and the proposed PnC with different ellipse errors (Section 4).

5.1. Dataset generation

To evaluate the accuracy of the benchmarked CBPE methods, we developed CRESENT - an extensive dataset consisting of 5,183 images that mimicked the expected conditions of a typical lunar orbiter surface surveillance mission [23]. Using PANGU [1], a planet and asteroid surface generation software, we loaded high-resolution DEMs from the PDS data node [25], and took Moon surface images at 100km altitude above areas of scientific interest, at angles increasing from $0°$ to $60°$ off nadir in increments of $10°$. Figures 2b - 2e consist of images taken from each of the four lunar regions. As neither CDAs nor CMAs were the focus of this work, both of these processes were simulated to return realistic crater detections with matched crater correspondences in Robbins' crater catalogue [28]. The implemented CDA filtered craters based on their 3D structure and projected ellipse appearance on the image plane and the CMA simulated incorrect crater matches introduced as a percentage of the number of available craters (keeping at the very least three correctly matched craters). Section 9 of the supplementary material provides more detail on image generation and how the CDA and CMA were simulated in this work.

5.2. Problem instances and evaluation metrics

All problem instances were initialised with the same noise to the crater detections and incorrect crater match correspondences. Given the ground truth $\mathbf{R}^{\ddagger}$ and $\mathbf{r}_M^{\ddagger}$ was known in the synthetic data, $\mathbf{R}^{\dagger}$ and $\mathbf{r}_M^{\dagger}$ was simulated in the range of $\mathbf{R}^{\ddagger} - \delta \leq \mathbf{R}^{\dagger} \leq \mathbf{r}_M^{\ddagger} + \delta$ and $\mathbf{r}_M^{\ddagger} - \gamma \leq \mathbf{r}_M^{\dagger} \leq \mathbf{r}_M^{\ddagger} + \gamma$ for each problem instance. For fair analysis of the PnP algorithm against the PnC methods, PnP was also provided with this same priori information.

To test the robustness of the benchmarked methods, the percentage of incorrectly matched outliers was increased. The attitude and position uncertainties were also increased, with δ and γ initialised to values of $0.01°$ and 6.7km ([21, 22] with justification in Sec. 10 of the supplementary material) and increased to uncertainties of $0.1°$ and 100km respectively.

The pose estimation algorithms were benchmarked using the following evaluation metrics:

- **observed surface error (m):** $|\mathbf{s}_M^{\ddagger} - \mathbf{s}_M{}^{*}|$
  The observed surface error was measured as the absolute distance between the two points produced by the intersection of the Moon's surface with the ground truth camera's line of sight vector and the estimated camera's line of sight vector (see Sec. 11 in the supplementary material).
- **position error (m):** $|\mathbf{r}_M^{\ddagger} - \mathbf{r}_M{}^{*}|$
  The position error was measured as the absolute distance between the ground truth camera position and the estimated camera position.
- **angular error (deg):** $\arccos\left((\mathrm{Tr}(\mathbf{R}^{\ddagger}.\mathbf{R}^{*T}) - 1)/2\right)$
  The angular error was measured as the absolute angular difference between the ground truth camera rotation and the estimated camera rotation.

5.3. Initialisation and hyperparameters for PnC

$\mathbf{R}_M^{(0)}$ and $\mathbf{r}_M^{(0)}$ were both randomly initialised in the range of $\mathbf{R}^{\dagger} - \delta \leq \mathbf{R}_M^{(0)} \leq \mathbf{r}_M^{\dagger} + \delta$ and $\mathbf{r}_M^{\dagger} - \gamma \leq \mathbf{r}_M^{(0)} \leq \mathbf{r}_M^{\dagger} + \gamma$ for each problem instance. The inlier threshold ϵ in Tukey's loss function (31) was also uniquely tuned for each metric.

5.4. Results on a reduced dataset

The benchmarked methods were initially evaluated on a reduced dataset consisting of 140 images from each of the four surface locations in CRESENT, with 20 images from each angle off nadir per surface. Every problem instance was captured in its best-case scenario, *i.e.* perfect crater matches and position and angular uncertainties of 6.7km and $0.01°$ respectively. The quantitative results for these experiments can be seen in table 1 and qualitative results can be seen in Figure 5 in the supplementary material.

For completeness, 3DoF_LS was included in the benchmarked methods, however, from these results we can see that the error introduced into the attitude initialisation affected the position accuracy, highlighting the importance of being able to refine both attitude and position for pose estimation. PnP has the second-highest observed surface error, demonstrating that the geometrical inconsistencies of PnP contribute an additional 135.5m on average to the observed surface error from the geometrically correct ED met-

	observed surface error (m)	position error (m)	angular error (deg)	runtime (s)
3DoF_LS	477.15	754.67	-	0.06
PnP	403.03	584.96	0.02	0.35
ECP	328.27	679.42	0.02	3.80
EP	247.84	437.42	0.02	4.10
ED	267.53	476.93	0.01	5.24
Gauss_Ang	301.72	536.94	0.02	5.68
L_Set	305.87	540.52	0.01	13.88
Wass	267.37	474.55	0.02	8.46

Table 1. Avg. results on the reduced dataset with perfect crater matches and position and angular uncertainties of 6.7 km and 0.01° respectively.

ric. While ED and L_Set are the only two metrics to noticeably improve the angular error, EP is the top-performing metric, improving the position and observed surface measurements by more than 147m and 155m respectively from the traditionally invoked CBPE methods.

On the same restricted dataset, we introduced 10% incorrect crater matches per image and obtained quantitative results (table 2) and qualitative results (Figures 2f and 2g - expanded in Figure 6 of the supplementary material).

	observed surface error (m)	position error (m)	angular error (deg)	runtime (s)
3DoF_LS	17564.27	39356.40	-	0.08
PnP	521.62	870.57	0.02	1.67
ECP	344.53	725.99	0.02	14.24
EP	278.17	514.19	0.02	16.09
ED	298.97	565.07	0.01	18.46
Gauss_Ang	342.62	618.67	0.02	16.43
L_Set	498.92	924.28	0.01	94.63
Wass	480.44	763.88	0.02	49.79

Table 2. Avg. results on the reduced dataset with 10% incorrect crater matches and position and angular uncertainties of 6.7 km and 0.01° respectively.

From these results, we can see the negative effect of not dealing with incorrect matches on the pose estimates, with 3DoF_LS resulting in a 3581.1% increase in observed surface error and a 5115.0% increase in position error. In contrast, EP only obtained a 12.2% increase in observed surface error and a 17.6% increase in position error. A box and whisker plots of the position error are shown in Figure 3 to further evaluate the effects of incorrect crater matches into the data. These plots support results from tables 1 - 2 and also highlight the variations in accuracy of the methods.

The bar charts in Figure 3 demonstrate the relationship between the position error and angle off nadir. From these bar charts, the optimal angle for most metrics is 20 degrees off nadir, with a trend in increasing position error for oblique viewing angles. This is supported by Figure 7a in the supplementary material which demonstrates that the highest crater distribution per problem instance occurs at 20° off nadir. The charts in Figure 3 plot the average position error against the number of craters used per problem instance, with a trend in lower position errors correlating to a larger number of detected craters (with viewing angles of 40° off nadir producing the largest number of detectable craters per problem instance on average - see Figure 7b in the supplementary material). From these charts, it is apparent that in addition to 3Dof_LS and PnP, ECP, L_Set and Wass are the least accurate and stable ellipse errors.

5.5. Evaluation on CRESENT

In the reduced dataset, EP, ED and Gauss_Ang consistently produced the most accurate and stable results. These metrics were tested on the full dataset, evaluating their performance under an increasing number of outlier crater matches and greater uncertainties in the *a priori* information.

Table 3 contains the average position error and observed surface error results over the full CRESENT dataset for small uncertainties (6.7km, 0.01°) and large uncertainties (100km, 0.1°). From the results produced under small uncertainties, EP outperforms all other metrics, achieving on average $\sim$300m observed surface accuracy and $\sim$600m position accuracy, even when 90% of the crater matches are outliers (implying three craters were used on average to estimate pose - see Figure 8 in the supplementary material). While increasing the uncertainty significantly increases the average position and observed surface errors across all metrics, we observe through Figure 4 that the median observed surface error for EP is $\sim$300m, and the average observed surface error is a consequence of very large outlier results due to the large attitude and position uncertainties.

From these results we can conclusively state the proposed PnC algorithm invoking the EP ellipse distance metric achieves the most accurate pose and observed surface measurement results for CBPE and significantly outperforms traditionally invoked LS and PnP methods.

(a) Average observed surface error (m) with small uncertainties.

% incorrect matches	0	10	20	30	40	50	60	70	80	90
EP	239.74	279.10	279.09	280.13	284.53	305.08	317.47	329.63	331.18	331.20
ED	263.82	307.34	307.32	308.37	312.85	335.18	348.35	360.64	362.92	362.89
Gauss_Ang	287.00	327.89	327.91	328.94	333.18	354.24	368.17	382.54	385.80	385.92

(b) Average position error (m) with small uncertainties.

% incorrect matches	0	10	20	30	40	50	60	70	80	90
EP	409.16	491.43	491.41	493.15	501.05	543.65	570.06	598.74	602.23	602.29
ED	452.56	544.69	544.68	546.39	554.39	600.41	631.71	661.81	667.54	667.64
Gauss_Ang	510.61	601.16	601.24	603.21	611.72	662.47	696.08	727.36	735.35	735.65

(c) Average observed surface error (m) with large uncertainties.

% incorrect matches	0	10	20	30	40	50	60	70	80	90
EP	1524.13	1588.47	1588.46	1623.35	1552.26	1946.84	2675.62	4074.11	4330.19	4314.16
ED	1309.34	1882.32	1882.32	1928.32	1866.43	3061.19	4426.20	6679.55	6981.91	6976.69
Gauss_Ang	44993.53	54350.47	54364.41	54388.61	56169.68	60475.93	61947.64	63562.19	63737.18	63724.82

(d) Average position error (m) with large uncertainties.

% incorrect matches	0	10	20	30	40	50	60	70	80	90
EP	3051.35	3375.45	3375.45	3386.31	3412.53	4024.70	5285.50	7778.96	8287.56	8260.29
ED	2758.33	4580.92	4580.99	4613.49	4612.03	8002.94	11801.13	16894.76	17607.96	17603.07
Gauss_Ang	44150.20	54421.97	54430.80	54534.51	56194.42	60711.94	62229.38	63892.60	64010.37	64005.88

Table 3. Results of metrics under small ($6.7km$, 0.01°) and large ($100km$, 0.1°) uncertainties.

6. Conclusion

The CBPE pipeline has promise of producing pose estimates that are desirable of lunar survey missions that re-

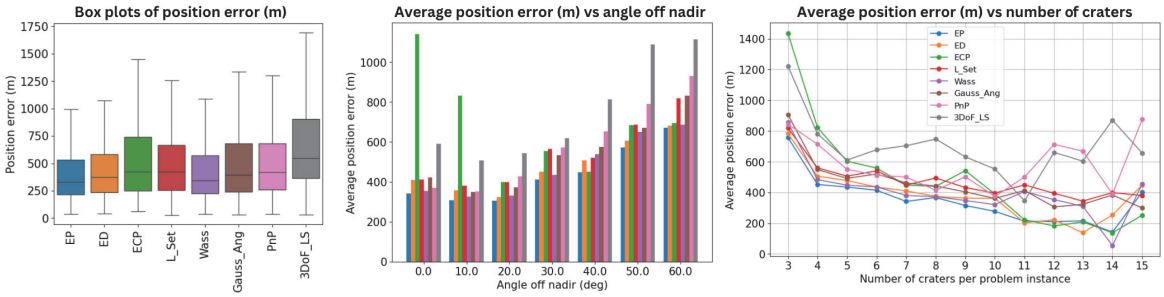

(a) Position error results on the reduced dataset with correct matches

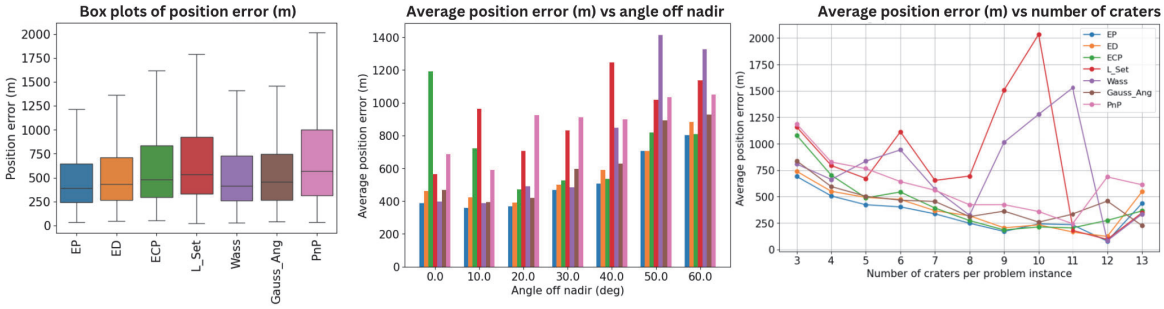

(b) Position error results on the reduced dataset with 10% incorrect matches

Figure 3. (a)(b) Position error results on the reduced dataset with correct matches (a) and 10% incorrect matches (b). Note that 3DoF_LS results were excluded from (b) due to the errors being too large (see table 2).

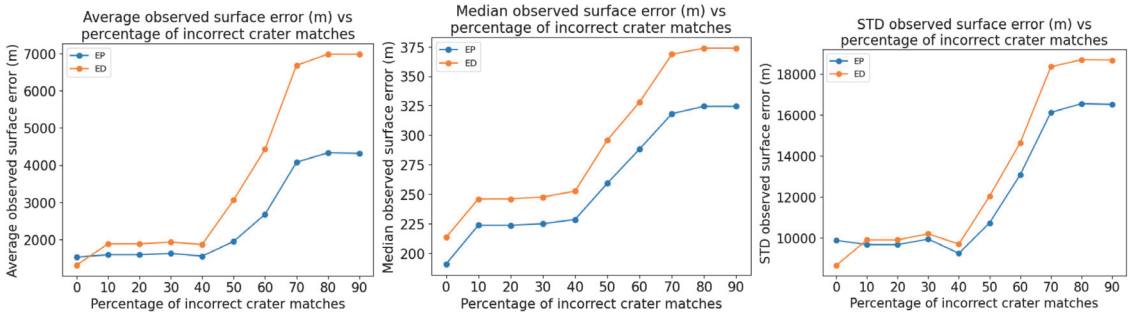

(a) (b) (c)

Figure 4. Average (a), median (b) and standard deviation (c) of the observed surface error over an increasing % of incorrect crater matches for the EP and ED metrics with large uncertainties. Note that Gauss_Ang was excluded as the resulting errors were too large (see table 3c).

quire highly accurate observed surface measurements. The final pose estimation step of the CBPE pipeline has had the least amount of development, with methods ranging from LS solvers that assume known attitude and do not compensate for outlier crater matches, to PnP algorithms that utilise geometrically incorrect 2D-3D crater correspondences. To address the drawbacks of these methods, we proposed robust PnC for CBPE. By benchmarking the CRESENT dataset, we conclusively demonstrate the limitations of the traditionally invoked pose estimation methods for CBPE and demonstrate significant improvements in position and observed surface measurement accuracy for the proposed PnC method.

7. Acknowledgements

Sofia Mcleod was supported by the Australian Government RTP Scholarship.

References

[1] Planet and asteroid natural scene generation utility product website. .https://pangu.software/ [Accessed: (01/12/2023)]. 6

[2] Zihao Chen and Jie Jiang. Crater detection and recognition method for pose estimation. *Remote Sensing*, 13(17):3467, 2021. 2, 4

[3] Yang Cheng and JK Miller. Autonomous landmark based spacecraft navigation system. 2003. 2

[4] John A Christian, Harm Derksen, and Ryan Watkins. Lunar crater identification in digital images. *J. Astronaut. Sci.*, 68 (4):1056–1144, 2021. 1, 2, 3, 4, 5

[5] The SciPy community. scipy.optimize.fmin_l_bfgs_b. https://docs.scipy.org/doc/scipy/reference/generated/scipy.optimize.fmin_l_bfgs_b.html, 2024. 5

[6] Roberto Del Prete and Alfredo Renga. A novel Visual-Based terrain relative navigation system for planetary applications based on mask R-CNN and projective invariants. *Aerotecnica Missili & Spazio*, 101(4):335–349, 2022. 1, 2

[7] D M DeLatte, S T Crites, N Guttenberg, and T Yairi. Automated crater detection algorithms from a machine learning perspective in the convolutional neural network era. *Adv. Space Res.*, 64(8):1615–1628, 2019. 2

[8] Wouter Doppenberg. *Autonomous lunar orbit navigation with Ellipse R-CNN*. PhD thesis, Delft University of Technology, 2021. 2, 4

[9] Lena Downes, Ted J Steiner, and Jonathan P How. Deep learning crater detection for lunar terrain relative navigation. In *AIAA Scitech 2020 Forum*. 2020. 2

[10] Todd A Ely, Jill Seubert, Nicholas Bradley, Ted Drain, and Shyam Bhaskaran. Radiometric autonomous navigation fused with optical for deep space exploration. *The Journal of the Astronautical Sciences*, 68:300–325, 2021. 1

[11] Martin A Fischler, SRI International Menlo Park CA Artificial Intelligence Center., and Robert C Bolles. *Random sample consensus: a paradigm for model fitting with applications to image analysis and automated cartography*. 1980. 2

[12] Chad Hanak and Timothy Crain. Crater identification algorithm for the lost in low lunar orbit scenario. Technical Report JSC-CN-18819, 2010. 2

[13] Francis Chad Hanak. *Lost in low lunar orbit crater pattern detection and identification*. PhD thesis, 2009. 2

[14] Andrew E. Johnson and James F. Montgomery. Overview of terrain relative navigation approaches for precise lunar landing. In *2008 IEEE Aerospace Conference*, pages 1–10, 2008. 1

[15] Hannah Kaufmann, Martin Lingenauber, Tim Bodenmueller, and Michael Suppa. Shadow-based matching for precise and robust absolute self-localization during lunar landings. In *2015 IEEE Aerospace Conference*, pages 1–13. IEEE, 2015. 1, 2

[16] M R Klear. Pycda: An open-source library for automated crater detection. *of the 9th Planetary Crater Consort, Boulder, CO, USA*. 2

[17] Vincent Lepetit, Francesc Moreno-Noguer, and Pascal Fua. EPnP: An accurate o(n) solution to the PnP problem. *Int. J. Comput. Vis.*, 81(2):155–166, 2009. 4

[18] C.C. Liebe. Accuracy performance of star trackers - a tutorial. *IEEE Transactions on Aerospace and Electronic Systems*, 38(2):587–599, 2002. 2, 4

[19] David A. Lorenz, Ryan Olds, Alexander May, Courtney Mario, Mark E. Perry, Eric E. Palmer, and Michael Daly. Lessons learned from osiris-rex autonomous navigation using natural feature tracking. In *2017 IEEE Aerospace Conference*, pages 1–12, 2017. 1

[20] Tingting Lu, Weiduo Hu, Chang Liu, and Daguang Yang. Relative pose estimation of a lander using crater detection and matching. *Organ. Ethic.*, 55(2):023102, 2016. 2, 4

[21] Bolko Maass, Svenja Woicke, Willem M Oliveira, Bronislovas Razgus, and Hans Krüger. Crater navigation system for autonomous precision landing on the moon. *Journal of Guidance, Control, and Dynamics*, 43(8):1414–1431, 2020. 1, 2, 4, 6

[22] Yoshikawa Makoto and Nishimura Toshimitsu. Current and future status of orbital determination of spacecraft in deep space. *Journal of The Society of Instrument and Control Engineers*, 39(9):564–569, 2000. 4, 6, 2

[23] Erwan Mazarico, D D Rowlands, G A Neumann, D E Smith, M H Torrence, F G Lemoine, and M T Zuber. Orbit determination of the lunar reconnaissance orbiter. *J. Geodesy*, 86 (3):193–207, 2012. 6

[24] NASA. The advantage of terrain relative navigation — nasa, 2024. Accessed: 2024-03-09. 1

[25] Massachusetts Institute of Technology. Lola pds data node. https://imbrium.mit.edu/ [Accessed: (05/26/2023)]. 1, 6

[26] Makiko Ohtake, Junichi Haruyama, Tsuneo Matsunaga, Yasuhiro Yokota, Tomokatsu Morota, Chikatoshi Honda, and LISM team. Performance and scientific objectives of the SELENE (KAGUYA) multiband imager. *Earth Planets Space*, 60(4):257–264, 2008. 1

[27] Woosang Park, Youeyun Jung, Hyochoong Bang, and Jaemyung Ahn. Robust crater triangle matching algorithm for planetary landing navigation. *Journal of Guidance, Control, and Dynamics*, 42(2):402–410, 2019. 2

[28] Stuart Robbins. Lunar crater database. https://doi.org/10.1029/2018JE005592. 6

[29] Stuart J Robbins. A new global database of lunar impact craters >1–2 km: 1. crater locations and sizes, comparisons with published databases, and global analysis. *J. Geophys. Res. Planets*, 124(4):871–892, 2019. 1, 2, 3

[30] M S Robinson, S M Brylow, M Tschimmel, D Humm, S J Lawrence, P C Thomas, B W Denevi, E Bowman-Cisneros, J Zerr, M A Ravine, M A Caplinger, F T Ghaemi, J A Schaffner, M C Malin, P Mahanti, A Bartels, J Anderson, T N Tran, E M Eliason, A S McEwen, E Turtle, B L Jolliff, and H Hiesinger. Lunar reconnaissance orbiter camera (LROC) instrument overview. *Space Sci. Rev.*, 150(1):81–124, 2010. 1

[31] G Salamunićcar and S Lončarić. Open framework for objective evaluation of crater detection algorithms with first test-

field subsystem based on MOLA data. *Adv. Space Res.*, 42 (1):6–19, 2008. 2

[32] Ari Silburt, Mohamad Ali-Dib, Chenchong Zhu, Alan Jackson, Diana Valencia, Yevgeni Kissin, Daniel Tamayo, and Kristen Menou. Lunar crater identification via deep learning. *Icarus*, 317:27–38, 2019. 2

[33] Erdem Turan, Stefano Speretta, and Eberhard Gill. Autonomous navigation for deep space small satellites: Scientific and technological advances. *Acta Astronautica*, 193: 56–74, 2022. 1

[34] Hao Wang, Jie Jiang, and Guangjun Zhang. CraterIDNet: An End-to-End fully convolutional neural network for crater detection and identification in remotely sensed planetary images. *Remote Sensing*, 10(7):1067, 2018. 2

[35] Svenja Woicke, Andres Moreno Gonzalez, Isabelle El-Hajj, Jelle Mes, Martin Henkel, and Robert Klavers. Comparison of Crater-Detection algorithms for Terrain-Relative navigation. In *2018 AIAA Guidance, Navigation, and Control Conference*. 2018. 2

[36] David Wokes and Stephen Wokes. Surveying and pose estimation of a lander using approximative crater modelling. In *AIAA Guidance, Navigation, and Control Conference*. 2010. 1, 2

[37] Yi Xiu, Shengying Zhu, Rui Xu, and Maodeng Li. Optimal crater landmark selection based on optical navigation performance factors for planetary landing. *Chin. J. Aeronaut.*, 36 (3):254–270, 2023. 2, 4

[38] Liheng Xu, Jie Jiang, and Yan Ma. Ellipse crater recognition for Lost-in-Space scenario. *Remote Sensing*, 14(23):6027, 2022. 2, 4

[39] Meng Yu, Hutao Cui, and Yang Tian. A new approach based on crater detection and matching for visual navigation in planetary landing. *Advances in Space Research*, 53(12): 1810–1821, 2014. 2

[40] Meng Yu, Shuang Li, Shuquan Wang, and Xiangyu Huang. Single crater-aided inertial navigation for autonomous asteroid landing. *Adv. Space Res.*, 63(2):1085–1099, 2019. 5

[41] Zhengyou Zhang. Parameter estimation techniques: a tutorial with application to conic fitting. *Image and Vision Computing*, 15(1):59–76, 1997. 5

[42] Shengying Zhu, Yi Xiu, Ning Zhang, Rui Xu, and Pingyuan Cui. Crater-based attitude and position estimation for planetary exploration with weighted measurement uncertainty. *Acta Astronaut.*, 176:216–232, 2020. 2

[43] Matthieu Zins, Gilles Simon, and Marie-Odile Berger. Level Set-Based camera pose estimation from multiple 2D/3D Ellipse-Ellipsoid correspondences. In *2022 IEEE/RSJ International Conference on Intelligent Robots and Systems (IROS)*, pages 939–946, 2022. 4, 5